Earthquakes and Structures, *Vol. 19, No. 2 (2020) 129-144*
DOI: https://doi.org/10.12989/eas.2020.19.2.129

Sloped rolling-type bearings designed with linearly variable damping force

Shiang-Jung Wang*, Yi-Lin Sung and Jia-Xiang Hong

Department of Civil and Construction Engineering, National Taiwan University of Science and Technology, No.43, Sec.4, Keelung Rd., Taipei 10607, Taiwan

(Received March 25, 2020, Revised August 7, 2020, Accepted August 8, 2020)

Abstract. In this study, the idea of damping force linearly proportional to horizontal isolation displacement is implemented into sloped rolling-type bearings in order to meet different seismic performance goals. In addition to experimentally demonstrating its practical feasibility, the previously developed analytical model is further modified to be capable of accurately predicting its hysteretic behavior. The numerical predictions by using the modified analytical model present a good match of the shaking table test results. Afterward, several sloped rolling-type bearings designed with linearly variable damping force are numerically compared with a bearing designed with conventional constant damping force. The initial friction damping force adopted in the former is designed to be smaller than the constant one adopted in the latter. The numerical comparison results indicate that when the horizontal isolation displacement does not exceed the designed turning point (or practically when subjected to minor or frequent earthquakes that seldom have a great displacement demand for seismic isolation), the linearly variable damping force design can exhibit a better acceleration control performance than the constant damping force design. In addition, the former, in general, advantages the re-centering performance over the latter. However, the maximum horizontal displacement response of the linearly variable damping force design, in general, is larger than that of the constant damping force design. It is particularly true when undergoing a horizontal isolation displacement response smaller than the designed turning point and designing a smaller value of initial friction damping force.

Keywords: sloped rolling-type bearing; linearly variable damping; analytical model; shaking table test; acceleration control; residual displacement

1. Introduction

Sloped rolling-type bearings have been studied extensively and also applied practically in the past two decades owing to their unique feature – keeping constant horizontal acceleration transmitted to the to-be-protected object (Harvey and Kelly 2016). That is, designing sloped surfaces in contact with rollers (Tsai *et al*. 2007, Lee *et al*. 2010, Wang *et al*. 2014, 2017, 2019) or balls (Kasalanati *et al*. 1997, Vargas and Bruneau 2009) together with constant damping force can make the seismic isolators mechanically, in-plane exhibit a zero post-elastic stiffness performance. This feature, of course, can facilitate the performance-based design (Ghobarah 2001, Hwang *et al*. 2004) if the to-be-protected object is vulnerable when undergoing excessive vibration (or acceleration) during earthquakes. In other words, during the design procedure of an isolation system composed of sloped rolling-type bearings, once their sloping angle and the built-in or additional damping force have been determined, the maximum horizontal acceleration response of the to-be-protected object can then be easily decided based on the dynamic equation of motion derived in past relevant researches (Wang *et al*. 2017) without further performing time-consuming nonlinear dynamic analyses. However, this feature might cause the procedure for predicting their horizontal isolation displacement under a given seismic demand very different from and even more complicated than the equivalent lateral force procedure (Iwan and Gates 1979, Hadjian 1982, Hwang 1996) commonly used for most of seismic isolators that mechanically reveal bilinear hysteretic behavior (Kelly 1990).

Wang *et al*. (2019) conducted a series of nonlinear response history analyses to numerically study the horizontal displacement responses of sloped rolling-type bearings designed with different sloping angles and friction damping force under various ground motions. It was indicated that the larger the designed sloping angle and friction damping force, in particular of the latter, the smaller the resulted horizontal isolation displacement. However, the augment of sloping angles and friction damping force will result in larger (or worse) horizontal acceleration transmitted to the to-be-protected object. In other words, increasing sloping angles and friction damping force will enlarge the transmitted horizontal acceleration response, i.e. will sacrifice the acceleration control performance. Besides, an increase in friction damping force might cause an unacceptable self-centering performance, which will significantly affect the serviceability and functionality of the to-be-protected object. This issue really needs more

*Corresponding author, Associate Professor
E-mail: sjwang@mail.ntust.edu.tw
[a]Graduate Student
E-mail: m10705323@mail.ntust.edu.tw
[b]Graduate Student
E-mail: m10005303@mail.ntust.edu.tw

http://www.techno-press.com/journals/was&subpage=7 ISSN: 2092-7614 (Print), 2092-7622 (Online)

attention when the performances of the objects protected by sloped rolling-type bearings under minor, moderate, and major earthquakes are equally important.

In Makris and Chang's study (2000, 2002), the effectiveness of different energy dissipative mechanisms used in seismic isolation systems against near-fault pulse-like ground motions was numerically examined. The results showed that adopting friction damping, compared with viscous damping, could more effectively reduce displacement demands and suppress displacement amplification under the ground motions which possess a long pulse period close to the designed isolation period. However, inevitably, friction damping may cause permanent displacement of seismic isolation systems. In addition to designing a single suitable friction coefficient for friction-type dampers or seismic isolators against some specific ground motions considered (Jangid 2017), several variable friction damping mechanisms in a passive manner have been proposed to effectively reduce acceleration and displacement responses of seismic isolation systems subjected to different ground motions. In Tadjbakhsh and Lin's study (1987), a progressive increased frictional resistance was developed by tightening a set of friction plates. The numerical results presented that adopting the proposed mechanism, compared with the constant frictional resistance design, can have more reductions in acceleration and relative displacement transmissibility. A well-known case, which has already become a mature seismic-resistant product at present and has been widely applied in engineering practice, is the double (or triple) friction pendulum bearing (Fenz and Constantinou 2006, 2008, Abdollahzadeh and Darvishi 2017, Shahbazi and Taghikhany 2017, Yurdakul and Ates 2018). In addition to different friction coefficients to present variable energy dissipation capabilities, varying curvature radii to present different stiffness (restoring force) capabilities were also adopted to offer designers greater flexibility to optimize the seismic performances of friction pendulum bearings at different stages as much as possible. Besides, the residual displacement responses of the double friction pendulum bearing designed with different friction coefficients as well as its accumulation conditions were also numerically and experimentally investigated (Ponzo *et al*. 2017). In Panchal and Jangid's study (2008), a variable friction pendulum system, in which the friction force increased up to a certain value of displacement and then decreased with further increase in displacement, was proposed. Based on the numerical results, it was demonstrated that adopting the proposed variable friction pendulum system can effectively control the responses of seismically isolated buildings under near-fault ground motions. In Calvi *et al*.'s study (2008), the seismic performances of flat and curved sliding bearings designed with different sliding materials and frictional properties were numerically examined. The numerical results showed that their performances can be improved significantly compared with the conventional seismic isolation solutions, in light of their higher energy absorption capacity.

Therefore, sloped rolling-type bearings are mechanically modified to be equipped with linearly variable damping force in this study. That is, as the horizontal isolation displacement increases, the built-in friction damping force will be passively and linearly increased. The feasibility of the prototype design, first, is demonstrated experimentally. A modified analytical model considering linearly variable damping force, then, is proposed based on the original analytical model only considering constant damping force. The accuracy and applicability of the modified analytical model is verified through comparing its prediction with the shaking table tests. Moreover, to further discuss the advantages and disadvantages of sloped rolling-type bearings designed with linearly variable damping force, their numerical results are compared with those of sloped rolling-type bearings designed with conventional, constant damping force.

2. Prototype design with linearly variable damping force

2.1 Mechanical design

In Wang *et al*.'s previous researches (2014, 2017, 2019), sloped rolling-type bearings (denoted as SRB hereafter), as illustrated in Fig. 1, consisted of a set of upper, intermediate, and lower bearing plates together with two pairs of mutually orthogonal cylindrical rollers (sandwiched between the upper and intermediate bearing plates as well as between the intermediate and lower bearing plates, respectively). The constant friction damping force designed for SRB was practically realized by using the rubber pads which were attached to the side surfaces of the upper, intermediate, and lower bearing plates and whose curved surfaces slid against the flat stainless steel surfaces of the side plates. Since seal ball bearings were used for connecting the multiple cylindrical rollers in parallel with the side plates, they can have the same displacement response (or a synchronized motion) during external excitation. Based on the Coulomb friction law for simplicity, the sliding friction force was simplified as a dry friction problem and thus its magnitude can be assumed to be proportional to the normal force. The constant normal force required for the constant sliding friction between the rubber pads and flat stainless steel surfaces was equal to the reaction force produced by compressing the linear spring modules embedded in the side surfaces of the three bearing plates and installed behind the rubber pads. Note that two linear spring modules were installed behind each rubber pad, and totally two rubber pads slid against each side plate. In addition, totally two parallel side plates were respectively connected with two ends of a pair of cylindrical rollers along each horizontal principle direction. It has been discussed in Wang *et al*.'s previous study (2014) that installing multiple (i.e., two or more) rollers in each horizontal principle direction was beneficial for the overall stability performance. Therefore, the total normal force, which was intended to produce the sliding friction force between a pair of parallel side plates and two opposite side surfaces of the upper and intermediate bearing plates (or the intermediate and lower bearing plates), was contributed by

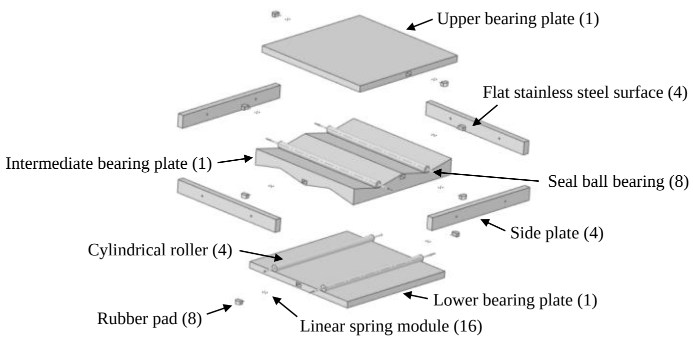

Fig. 1 Detailed decomposition of SRB-CDF (PS: the number in the parenthesis denotes the amount of the component used in a single bearing)

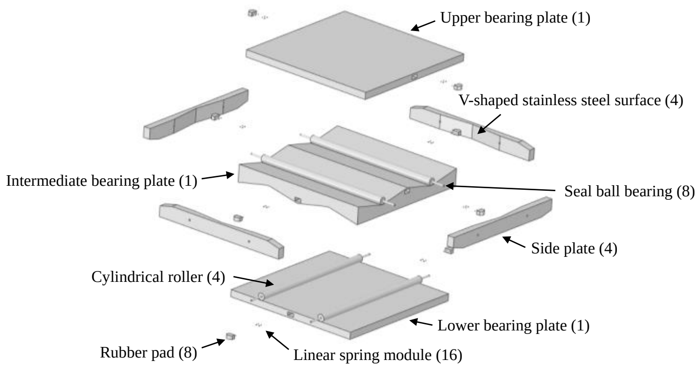

Fig. 2 Detailed decomposition of SRB-LVDF (PS: the number in the parenthesis denotes the amount of the component used in a single bearing)

compressing totally four linear spring modules in parallel. Linear spring modules can be effortlessly adjusted and replaced to meet different design requirements in engineering practice. Herein, SRB designed with constant damping force is denoted as SRB-CDF.

In this study, in order to design linearly variable damping force for SRB, the flat stainless steel surface, as shown in Fig. 1, is replaced by a V-shaped one, as illustrated in Fig. 2. Except for the damping force design, the remaining design mechanisms, basically, are identical to those proposed in Wang *et al*.'s previous researches (2014, 2017, 2019). By doing so, when there is no horizontal sliding displacement of the rubber pad relative to the V-shaped stainless steel surface (i.e., at the static condition), the constant normal force can still be provided by the initial shortening of the linear spring modules installed behind the rubber pad. More importantly, when the horizontal sliding displacement of the rubber pad relative to the V-shaped stainless steel surface increases, rationally neglecting the very limited elastic deformation of the rubber pad for simplicity, the shortening of linear spring modules, the resultant normal force, and the resultant friction damping force will be proportionally and linearly enlarged. Herein, SRB designed with linearly variable damping force is denoted as SRB-LVDF. If this mechanical design can be practically realized, adopting more complicated or combined functions other than a linear one to design the sliding surfaces of the side plates of SRB for diverse control performance goals of variable damping force could also be doable technically.

2.2 Modified analytical model

A simplified model for SRB-CDF at static and motion conditions, in which a single cylindrical roller is sandwiched between two V-shaped rolling surfaces designed with different sloping angles and constant friction damping force is designated, are illustrated in Figs. 3(a) - 3(b) (Wang *et al*. 2017), respectively. Through rationally linearizing the trigonometric functions during derivation since the sloping angles are usually designed as a considerably small value, when the roller is moving between two sloped surfaces (i.e., in the slope rolling range), the simplified equation of motion for the horizontal dynamic behavior of SRB-CDF under horizontal (or in-plane) excitation is obtained by (Wang *et al*. 2019)

$$\ddot{x}_1 + \ddot{x}_g = \frac{-1}{2} g\left(\theta_1 + \theta_2\right) \operatorname{sgn}\left(x_1\right) - \frac{F_D}{\left(M + m_1\right)} \operatorname{sgn}\left(\dot{x}_1\right) \quad (1)$$

where M, m_1, and m_2 are the seismic reactive masses of the protected object, superior bearing plate, and roller, respectively; r is the sectional radius of the roller; θ_1 and θ_2 are the sloping angles of the superior and inferior bearing plates, respectively (θ_1=0 and θ_2=0, respectively, represent that the surfaces of the superior and inferior bearing plates in contact with the roller are designed to be flat ones); $\ddot{x}_g(\ddot{z}_g)$ is the horizontal (vertical) acceleration excitation;, $x_1(z_1)$, $\dot{x}_1(\dot{z}_1)$ and $\ddot{x}_1(\ddot{x}_1)$ and are the horizontal (vertical) displacement, velocity, and acceleration responses of the protected object and superior bearing plate relative to the

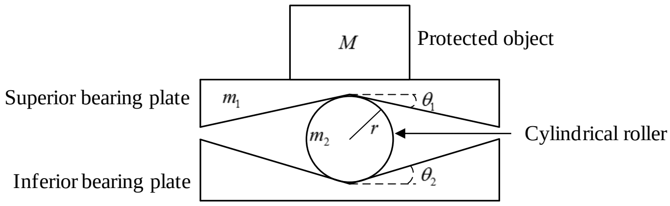

(a) static condition

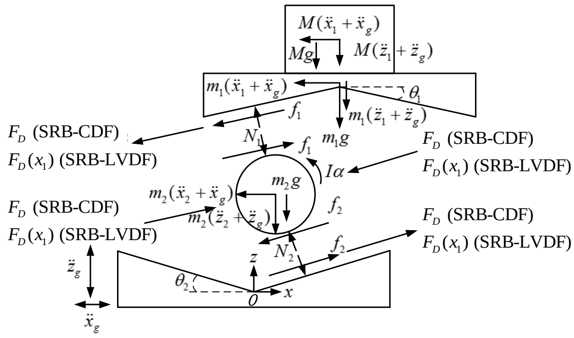

(b) free body diagrams when sgn(x_1)=sgn(x_2)=1 and sgn($\dot{x}_1$)=sgn($\dot{x}_2$)=1

Fig. 3 A simplified model for SRB-CDF and SRB-LVDF (Wang *et al*. 2017)

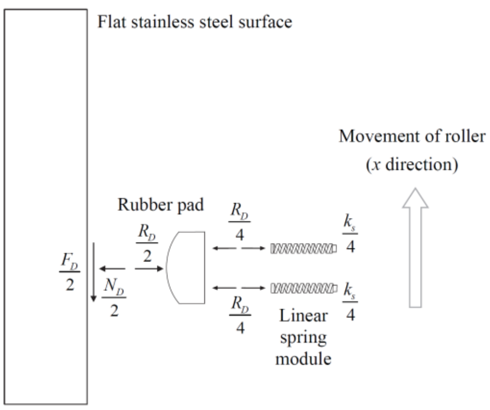

(a) SRB-CDF (with a flat sliding surface)

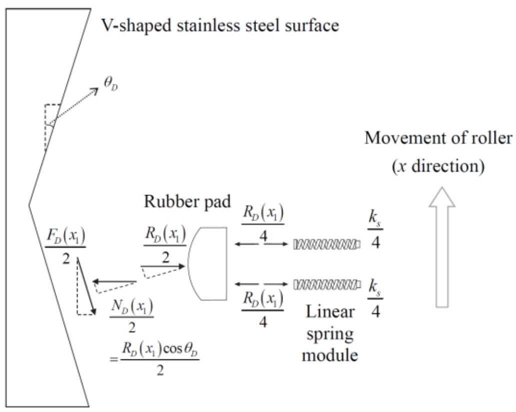

(b) SRB-LVDF (with a V-shaped sliding surface)

Fig. 4 Free body diagrams of two rubber pads and one sliding surface

origin O (or the inferior bearing plate), respectively; $x_2(z_1)$, $\dot{x}_2(\dot{z}_2)$ and $\ddot{x}_g(\ddot{x}_2)$.are the horizontal (vertical) displacement, velocity, and acceleration responses of the roller relative to the origin O (or the inferior bearing plate), respectively; the positive directions of x and z are correspondingly defined to be rightward and upward in the figure; g is the acceleration of gravity; I is the moment of inertia of the roller; α is the angular acceleration of the roller (the positive rotation is defined to be clockwise in the figure); $f_1(f_2)$ and $N_1(N_2)$ are the rolling friction force and normal force acting between the superior bearing plate and roller (between the roller and inferior bearing plate), respectively; and F_D is the total built-in friction damping force acting parallel to the slope of the bearing plates, which is proportional to the total normal force N_D and is produced by four rubber pads and a parallel pair of flat sliding surfaces. For simplicity in this study, the non-uniform friction distribution (Wei *et al*. 2017) which might cause different seismic responses is not considered. As observed from the free body diagram of two rubber pads and one flat sliding surface shown in Fig. 4(a) on which only $N_D/2$, $R_D/2$, and $F_D/2$ are exerted, the total reaction force R_D is produced by compressing the linear spring modules with a total elastic constant of k_s installed behind the rubber pads. Each linear spring module as shown in Fig. 4(a) has an elastic constant of $k_s/4$. If rationally assuming that the directions of gravitational force of the rubber pads and linear spring modules are perfectly perpendicular to those of N_D and R_D, the magnitude of N_D, theoretically, is equal to that of R_D. Note that since the sloping angles are usually designed as a considerably small value, the horizontal displacement of the protected object (or the superior bearing plate) relative to the inferior bearing plate, i.e., x_1, can be rationally approximated as twice as that of the roller (or the side plate) relative to the inferior bearing plate, i.e., x_2 (Lee *et al*. 2010, Wang *et al*. 2014). In other words, the horizontal displacement of the protected object (or the superior bearing plate) relative to the roller (or the side plate), i.e., x_1-x_2, is almost the same as that of the roller (or the side plate) relative to the inferior bearing plate, i.e., x_2.

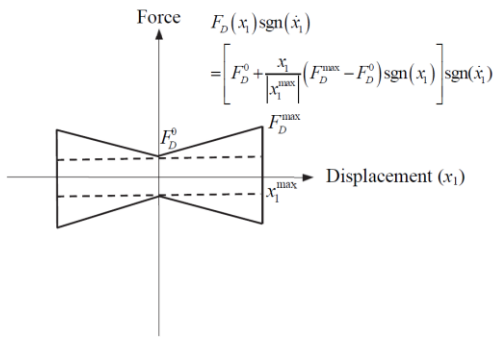

(a) $F_D(x_1)\mathrm{sgn}(\dot{x}_1)$ versus x_1 without considering effect arising from the normal force component

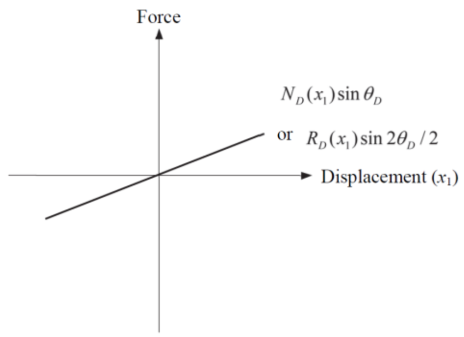

(b) the normal force component versus x_1

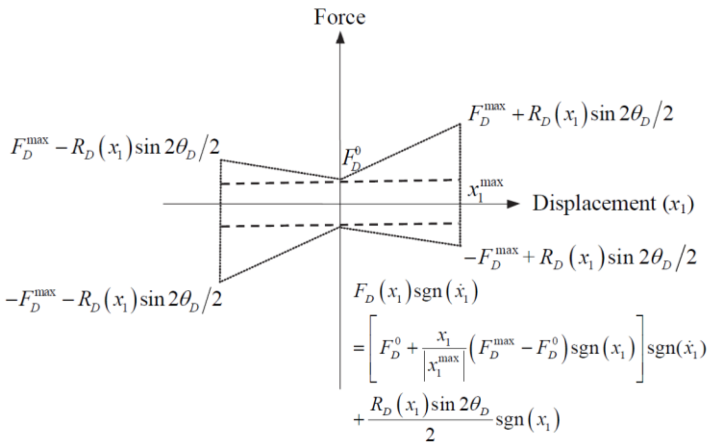

(c) $F_D(x_1)\mathrm{sgn}(\dot{x}_1)$ versus x_1 considering effect arising from the normal force component

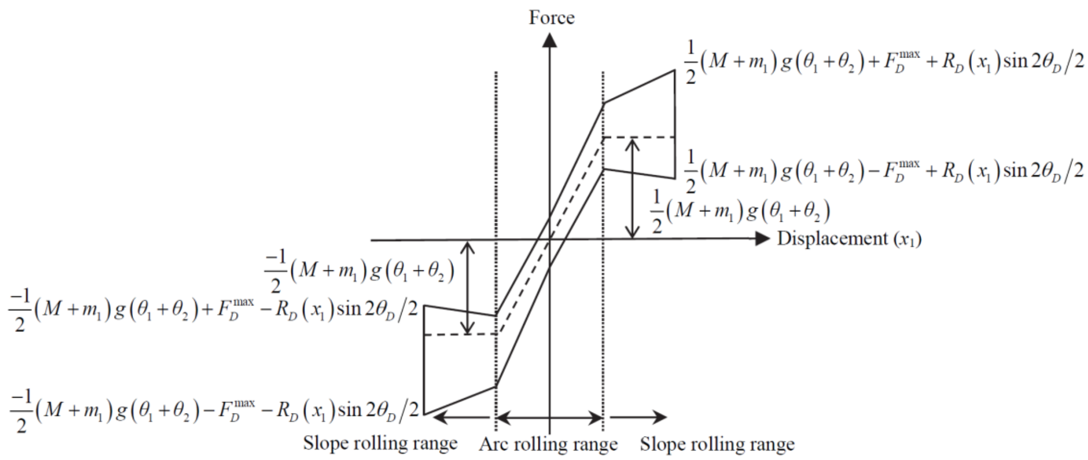

(d) hysteretic behavior of SRB-LVDF

Fig. 5 Illustration of modified analytical models for SRB-LVDF

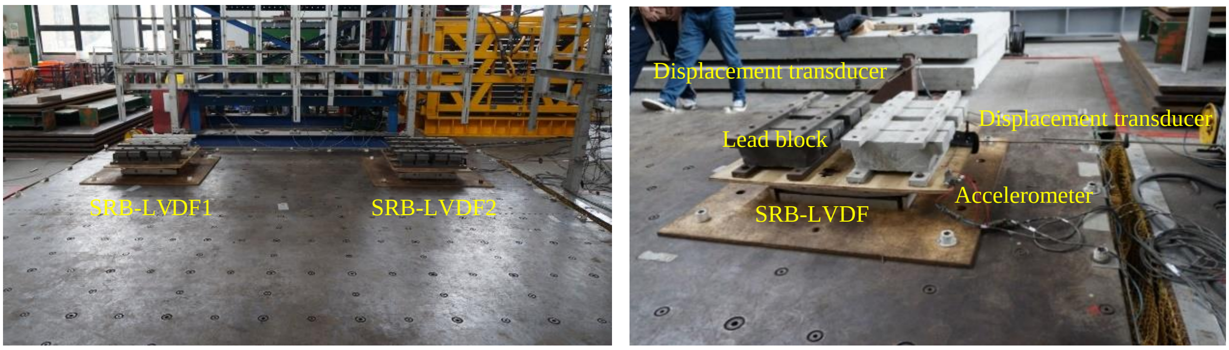

Fig. 6 Test installation

To not alter the previous design mechanism too much, the prototype of SRB-LVDF in this study is developed based on that of SRB-CDF. Different from SRB-CDF, the curved surfaces of rubber pads slide against a V-shaped surface with a constant slope of tan θ_D rather than a flat one. Therefore, the magnitude of the total built-in friction damping force during motion is a linear function of horizontal isolation displacement $F_D(x_1)$ rather than a constant F_D. As observed from the free body diagram of two rubber pads and one V-shaped sliding surface shown in Fig. 4(b) on which, $N_D(x_1)/2$, $R_D(x_1)/2$ and $F_D(x_1)/2$ are exerted, the total reaction force $R_D(x_1)$ is produced by compressing the linear spring modules with a total elastic constant of k_s installed behind the rubber pads. Each linear spring module as shown in Fig. 4(b) has an elastic constant of $k_s/4$. If rationally assuming that the directions of gravitational force of the rubber pads and linear spring modules are perfectly perpendicular to those of the total normal force $N_D(x_1)$ directed perpendicular to the sliding surfaces as well as $R_D(x_1)$, theoretically, $N_D(x_1)$ is a force component of $R_D(x_1)$, i.e., $N_D(x_1)=R_D(x_1)\cos\theta_D$.

The produced friction damping force can be resolved into two force components respectively directed parallel to and horizontally perpendicular to the x direction, as also shown in Fig. 4(b). Accordingly, the effective friction damping force directed parallel to the x direction varying with x_1 (or $2x_2$), i.e., $F_D(x_1)\mathrm{sgn}(\dot{x}_1)$, and its hysteresis loop are expressed by Eq. (2) and presented in Fig. 5(a), respectively.

$$F_D(x_1)\mathrm{sgn}(\dot{x}_1) = \left[F_D^0 + \frac{x_1}{\left|x_1^{\max}\right|}\left(F_D^{\max} - F_D^0\right)\mathrm{sgn}(x_1)\right]\mathrm{sgn}(\dot{x}_1) \tag{2}$$

where F_D^0 is the magnitude of the minimum (or initial) friction damping force produced by the initial shortening of the linear spring modules l_0 and F_D^{max} is the magnitude of the maximum friction damping force at the designed maximum horizontal displacement capacity $|x_1^{max}|$ (or at the maximum shortening of the linear spring modules l_{max}).

Furthermore, as also observed from Fig. 4(b), the horizontal force component of the total normal force directed perpendicular to the sliding surface, i.e., $N_D(x_1)\sin\theta_D$ or $R_D(x_1)\sin2\theta_D/2$, might have a non-negligible influence on the x-directional total friction damping force. Its variation with x_1(or $2x_2$) considering $\mathrm{sgn}(x_1)=\pm1$ is illustrated in Fig. 5(b). Therefore, the resultant force of the two force components as presented in Figs. 5(a) - 5(b) should be taken into consideration to represent the actual x-directional friction damping force performance of SRB-LVDF, as given in Eq. (3) and shown in Fig. 5(c).

$$F_D(x_1)\mathrm{sgn}(\dot{x}_1) = \left[F_D^0 + \frac{x_1}{\left|x_1^{\max}\right|}\left(F_D^{\max} - F_D^0\right)\mathrm{sgn}(x_1)\right]\mathrm{sgn}(\dot{x}_1) + \frac{R_D(x_1)\sin2\theta_D}{2}\mathrm{sgn}(x_1) \tag{3}$$

As observed from Fig. 5(c), because of the existence of the last term in Eq. (3), the proposed linearly variable damping force design mechanism will provide slightly larger force in the first and third quadrants, i.e., when $\mathrm{sgn}(x_1)$, $\mathrm{sgn}(\dot{x}_1)$ and $\mathrm{sgn}(x_1)$=-1, $\mathrm{sgn}(\dot{x}_1)$=-1, respectively, compared with that in the second and fourth quadrants, i.e. when $\mathrm{sgn}(\dot{x}_1)$=-1, $\mathrm{sgn}(\dot{x}_1)$=1 and $\mathrm{sgn}(x_1)$=1, $\mathrm{sgn}(\dot{x}_1)$=-1, respectively. Therefore, in the future study or application, if any other more complicated or combined functions, rather than simple ones such as a linear function discussed in this study, are implemented into SRB with the same design mechanism, it is noted that in addition to the produced friction damping force in the direction of interest, the force component of the normal force corresponding to the designed function in the direction of interest should also be taken into consideration to have more conservative and accurate numerical simulation.

Taking the pounding prevention mechanism suggested in Wang *et al.*'s previous study (2014) into consideration, an arc rolling range with a curvature radius (R) is provided at the intersection of two inclines of V-shaped surfaces in contact with rollers. When the roller is moving between a round surface with a fixed curvature radius and a flat surface as well as between two round surfaces with a fixed curvature radius (i.e., in the arc rolling range), the simplified equations of motion for the horizontal dynamic behavior of SRB-LVDF under horizontal (or in-plane) excitation are obtained by using Eqs. (4) and (5), respectively (Wang *et al*. 2014, 2017).

$$\ddot{x}_1 + \ddot{x}_g = -\frac{g}{4R}x_1 - \frac{F_D}{(M+m_1)}\mathrm{sgn}(\dot{x}_1) \tag{4}$$

$$\ddot{x}_1 + \ddot{x}_g = -\frac{g}{2R}x_1 - \frac{F_D}{(M+m_1)}\mathrm{sgn}(\dot{x}_1) \tag{5}$$

Based on the simplified equation of motion when the roller is moving on a round surface as given in Eq. (4) or (5), as well as that when the roller is moving between a sloped surface and a flat surface as given in Eq. (1), in which F_D is replaced by $F_D\mathrm{sgn}(\dot{x}_1)$ calculated as per Eq. (3), a modified analytical model for characterizing the horizontal hysteretic behavior of SRB-LVDF can be established, as illustrated in Fig. 5(d).

3. Experimental verification and numerical prediction of SRB-LVDF

3.1 Test specimens and protocol

Two SRB-LVDF specimens, denoted as SRB-LVDF1 and SRB-LVDF2 hereafter, consist of lower, intermediate, and upper bearing plates from bottom to top. There are two pairs of mutually orthogonal cylindrical rollers respectively sandwiched between the lower and intermediate bearing plates as well as between the intermediate and upper bearing plates. The surfaces of the lower (or upper) and intermediate bearing plates in contact with the rollers are designed to be flat and dual V-shaped with a sloping angle of 6 degrees, respectively. An arc rolling range of 12.6 mm

Table 1 Design parameters of test specimens and numerical models

Design parameter	Lower and upper (intermediate) bearing plates: Mass (kg)	Lower and upper (intermediate) bearing plates: Sloping angle (degrees)	$\lvert x_1^{max} \rvert$ (mm)	Arc rolling range(mm)	R (mm)	Friction damping force design	F_D^0 (N)	F_D^{max} (N)	μ_k	$\frac{R_D(x_1)\sin 2\theta_D}{2}$ at $\lvert x_1^{max} \rvert$ (N)
SRB-LVDF1			210			Linearly variable	110	180		40
SRB-LVDF2							180	560		340
SRB-CDF-250						Constant	250	250		0
SRB-CDF-50-50							50	705.2		544.8
SRB-LVDF-50-100							50	377.6		272.4
SRB-LVDF-50-150							50	268.4		181.6
SRB-LVDF-100-50	24.51 (29.44)	0 (6)	300	12.6	60		100	455.2	0.3	544.8
SRB-LVDF-100-100						Linearly variable	100	277.6		272.4
SRB-LVDF-100-150							100	218.4		181.6
SRB-LVDF-150-50							150	205.2		544.8
SRB-LVDF-150-100							150	177.6		272.4
SRB-LVDF-150-150							150	168.4		181.6

with a curvature radius of 60 mm is designed at the intersection of two inclines of V-shaped surfaces in contact with rollers. The maximum displacement capacity in each horizontal principle direction is ±210 mm, i.e., x_1^{max}=±210 mm. The seismic reactive masses of the lower (or upper) bearing plate, the intermediate bearing plate, and a single roller are 25.41 kg, 29.44 kg, and 4.58 kg, respectively. The sectional radius (r) of each cylindrical roller is 17.5 mm.

The total elastic constants of the four linear spring modules in parallel (k_s) designed for SRB-LVDF1 and SRB-LVDF2 are 8.5 N/mm and 15 N/mm, respectively. The initial shortening of linear spring modules (l_0) designed for SRB-LVDF1 at the equilibrium position is 11 mm, while that for SRB-LVDF2 is 10 mm. The V-shaped surfaces of the side plates sliding against the rubber pads for SRB-LVDF1 are designed with a slope ($\tan\theta_D$) of 0.067 (=l_{max}-l_0)/($|x_1^{max}|$/2)=7 mm/ 105 mm), while those for SRB-LVDF2 are designed with a slope of 0.19 (=l_{max}-l_0)/($|x_1^{max}|$/2)=20 mm/ 105 mm). In other words, when reaching the maximum horizontal displacement $|x_1^{max}|$/, the maximum shortening of linear spring modules (l_{max}) designed for SRB-LVDF1 is 18 mm, while that for SRB-LVDF2 is 30 mm. Referring to the past experimental identification results (Wang *et al*. 2014, 2017), the kinetic friction coefficient between the rubber and stainless materials (μ_k) adopted in SRB-CDF is approximated by a constant of 0.3. Thus, as per Eq. (3), the x-directional total friction damping force of SRB-LVDF1 (SRB-LVDF2) can then be designed to be linearly varied from 110 N (180 N) at the equilibrium position to 220 N (900 N) at the maximum horizontal displacement (when sgn(x_1)=1, sgn($\dot{x}_1$)=1 and sgn(x_1)=-1, sgn($\dot{x}_1$)=-1 and to 140 N (220 N) at the maximum horizontal displacement (when sgn(x_1)=-1, sgn(x_1)=1 and sgn(x_1)=1, sgn($\dot{x}_1$)=-1). The design parameters of SRB-LVDF1 and SRB-LVDF2 are summarized in Table 1.

The to-be-protected object above SRB-LVDF1 and SRB-LVDF2 is simulated by regularly arranged lead blocks with a total seismic reactive mass of 500 kg. The test setup on the shaking table, containing the two test specimens as well as accelerometers and displacement transducers installed for dynamic measurement, is presented in Fig. 6. Substituting the quantitative design parameters aforementioned into Eqs. (1), (3) and (4), the numerical hysteretic models of SRB-LVDF1 and SRB-LVDF2 can be obtained, as shown in Fig. 7.

As detailed in Table 2, three recorded ground motions obtained from the Pacific Earthquake Engineering Research (PEER) Ground Motion Database, denoted as El Centro, Kobe, and TCU129 hereafter, and one artificially generated acceleration history (Chai *et al*. 2002) compatible with the required response spectrum (RRS) specified in AC156 (2010), denoted as AC156 hereafter, are selected as the unilateral acceleration inputs. The 5% damped acceleration and displacement response spectra of these unilateral acceleration inputs with a peak acceleration (PA) value normalized to 1 g are shown in Fig. 8.

3.2 Test results

The measured horizontal acceleration and displacement response histories as well as the hysteresis loops of SRB-LVDF1 and SRB-LVDF2 under El Centro, Kobe, TCU129,

Table 2 Acceleration input programs for experimental and numerical study

Acceleration input		Input earthquake information or response spectrum condition	Excitation direction		PA (g)	Scale (%)
Recorded earthquake history	El Centro	IMPVALL/I-ELC180 Imperial Valley, U.S. 1940/05/19	Unilateral direction	Experimental study	0.35	100%
				Numerical study	0.175	50%
					0.35	100%
					0.525	150%
					0.7	200%
	Kobe	KOBE/KJM000 Kobe, Japan 1995/01/16		Experimental study	0.82	100%
				Numerical study	0.246	30%
					0.492	60%
					0.82	100%
					1.23	150%
	TCU 129	Chi-Chi/TCU129 Chi-Chi, Taiwan 1999/09/21		Experimental study	1.01	100%
				Numerical study	0.505	50%
					1.01	100%
					1.515	150%
					2.02	200%
Artificial acceleration history	AC 156	RRS specified in AC156 Isolated equipment is placed at 3rd floor (8.75m in elevation) of a 7-story building (24m in height) at Taipei City		Experimental study	0.62	100%
				Numerical study	0.31	50%
					0.62	100%
					0.93	150%
					1.24	200%

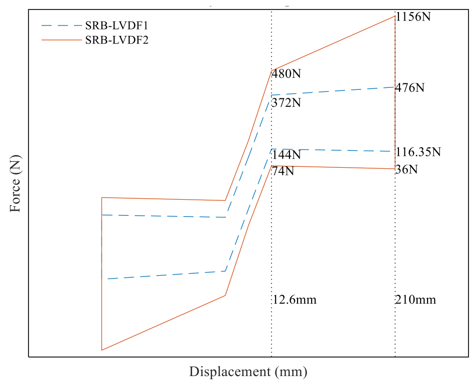

Fig. 7 Numerical hysteretic models of SRB-LVDF1 and SRB-LVDF2

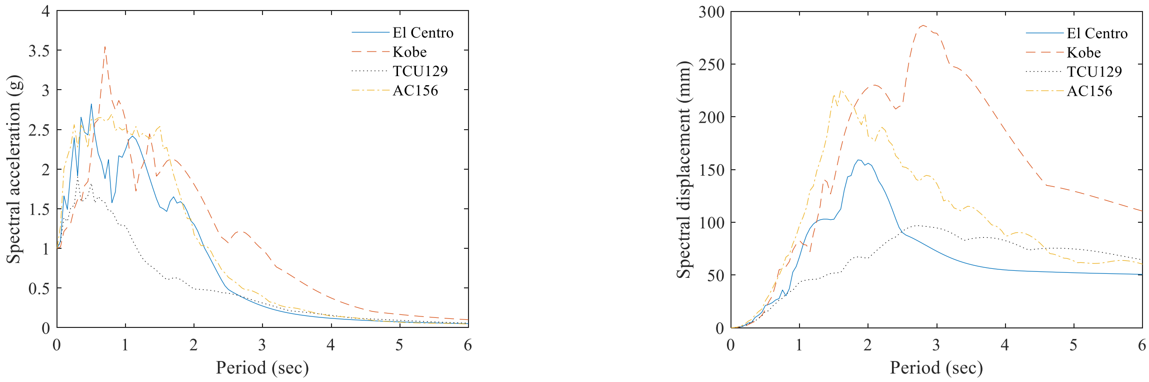

Fig. 8. 5% damped response spectra of selected unilateral acceleration inputs (PA=1 g) for experimental and numerical study

and AC156 are presented in Figs. 9 - 12, respectively. The quantitative information, including experimental maximum transmitted acceleration ($A_{max,test}$), experimental maximum isolation displacement ($D_{max,test}$), and experimental residual displacement ($D_{res,test}$) are also provided in these figures. Apparently, the acceleration transmitted to the protected object above either SRB-LVDF1 or SRB-LVDF2 can be well controlled and significantly reduced compared with the PA values of the unilateral acceleration inputs. More importantly, the experimental damping force is, as expected, linearly augmented with increasing the horizontal isolation displacement, i.e., x_1, although some fluctuations owing to

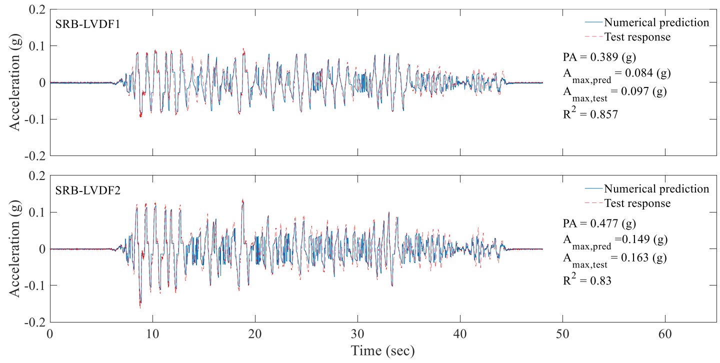

(a) acceleration response histories

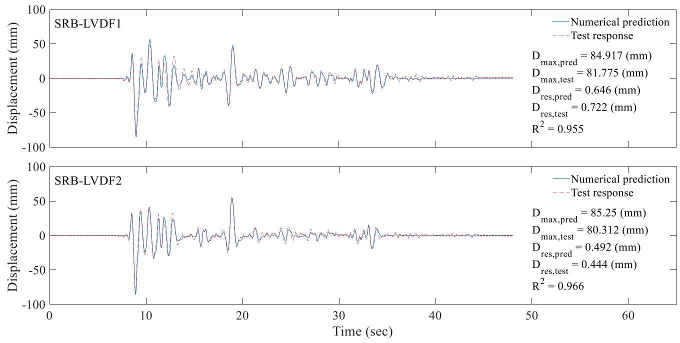

(b) displacement response histories

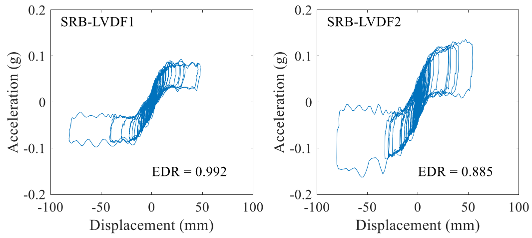

(c) hysteresis loops

Fig. 9 Experimental responses and numerical predictions of SRB-LVDF1 and SRB-LVDF2 under El Centro

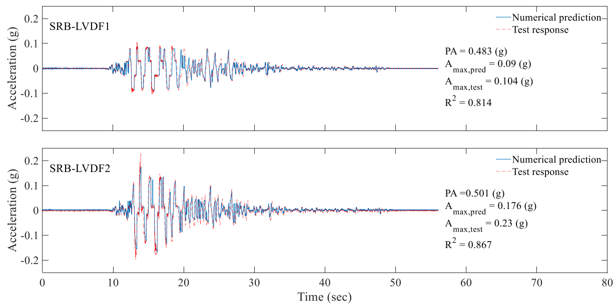

(a) acceleration response histories

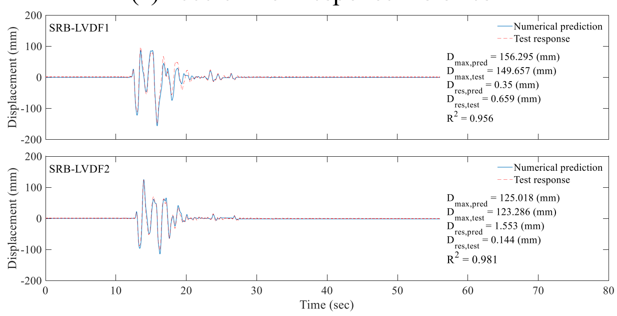

(b) displacement response histories

Fig. 10 Continued

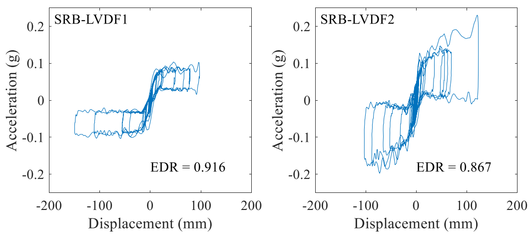

(c) hysteresis loops

Fig. 10 Experimental responses and numerical predictions of SRB-LVDF1 and SRB-LVDF2 under Kobe

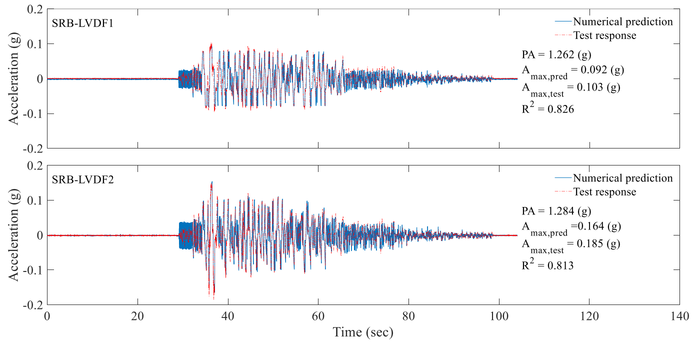

(a) acceleration response histories

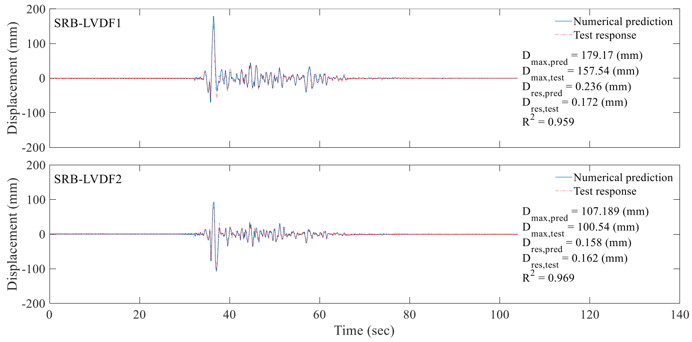

(b) displacement response histories

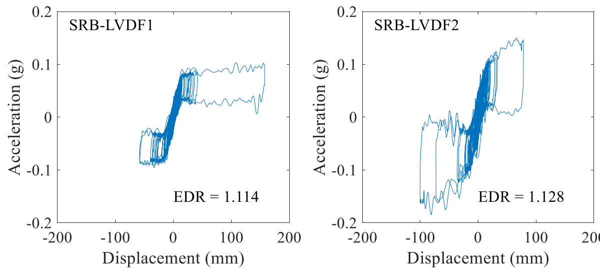

(c) hysteresis loops

Fig. 11 Experimental responses and numerical predictions of SRB-LVDF1 and SRB-LVDF2 under TCU129

the breakaway friction effect at initiation of sliding (Constantinou *et al*. 1990) are inevitable, which still needs further mechanical improvement or more precise simulation in the future. In other words, the test results demonstrate that the proposed linearly variable damping force design in a passive control manner can be implemented into SRB. As a consequence, the design of SRB-LVDF is practically feasible. In addition, after external disturbance, both SRB-LVDF1 and SRB-LVDF2 have very limited residual displacement, which indicates that SRB-LVDF can have a very satisfactory re-centering performance. Under all the unilateral acceleration inputs, the maximum horizontal displacement responses do not exceed the maximum displacement capacity of SRB-LVDF1 and SRB-LVDF2, i.e., 210 mm.

As introduced before and as can be observed from Fig. 7, SRB-LVDF1 is provided with lower values of F_D^0 and F_D^{max} as well as a lower slope of the total friction damping force varying with x_1 (or $2x_2$) than SRB-LVDF2. Thus, the test results are coincident with the design expectations, i.e., compared with SRB-LVDF2 under the same external disturbance, SRB-LVDF1, in general, has a better

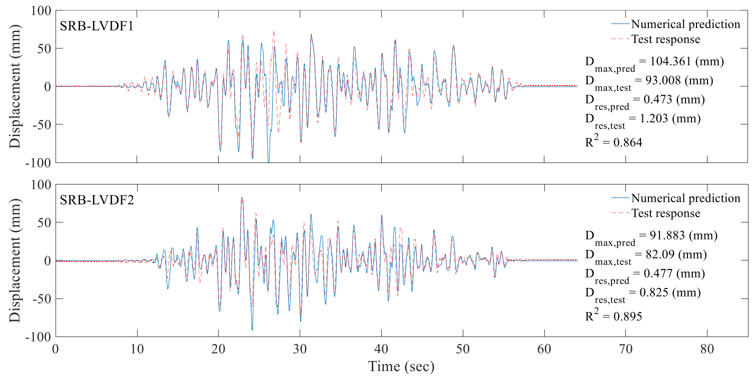

(b) displacement response histories

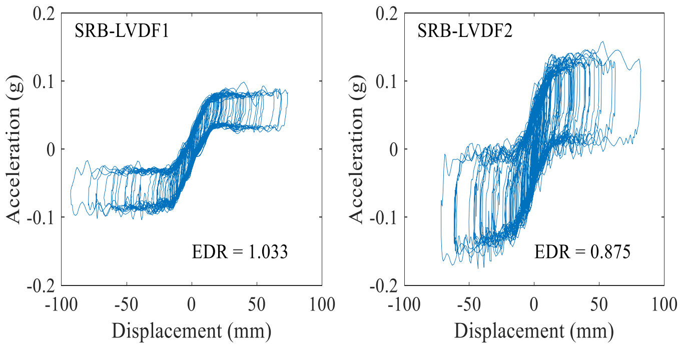

(c) hysteresis loops

Fig. 12 Experimental responses and numerical predictions of SRB-LVDF1 and SRB-LVDF2 under AC156

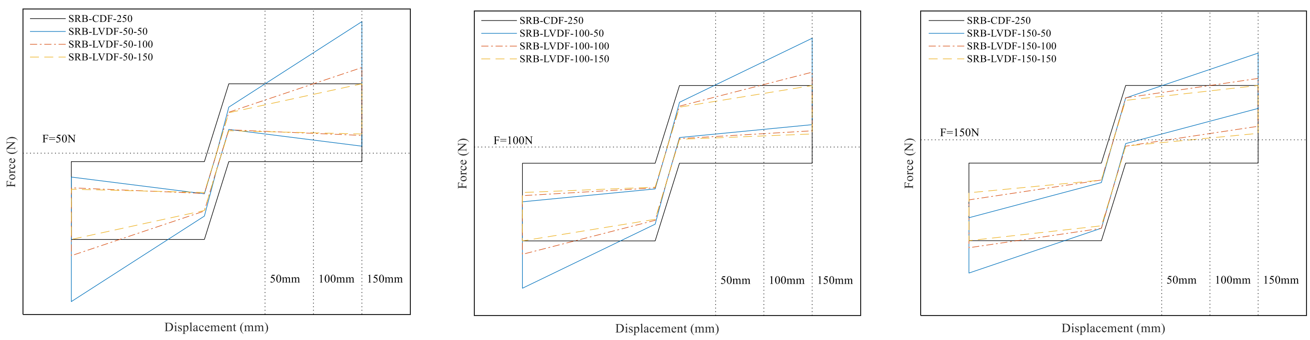

(a) SRB-LVDF-50-50, -50-100, -50-150 and SRB-CDF-250

(b) SRB-LVDF-100-50, -100-100, -100-150 and SRB-CDF-250

(c) SRB-LVDF-150-50, -150-100, -150-150 and SRB-CDF-250

Fig. 13 Numerical hysteretic models of one SRB-CDF model and nine SRB-LVDF models

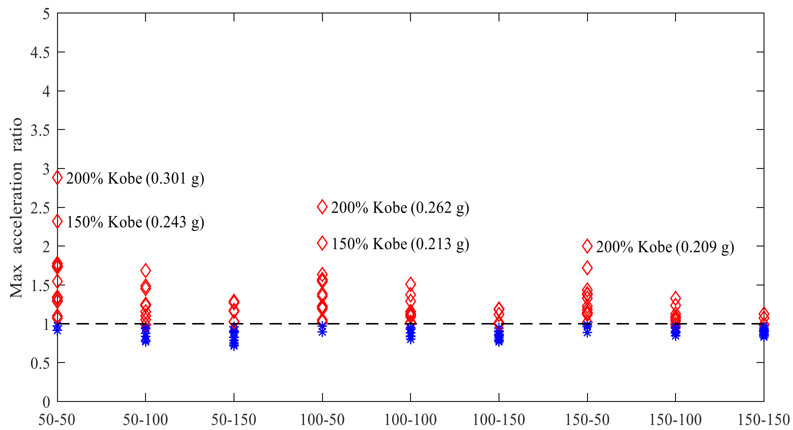

Fig. 14 Comparison of predicted maximum transmitted acceleration between SRB-CDFand SRB-LVDF models

acceleration control performance (or smaller acceleration response) but a worse performance in suppressing displacement (or a larger maximum displacement response).

3.3 Numerical verification

By means of the author-developed analysis program, in which the step-by-step integration method, different equations of motions at different stages, and the relative static state (or sticking phase) are appropriately considered (Wang *et al.* 2017, 2019), the dynamic responses of SRB-LVDF1 and SRB-LVDF2 under external disturbance can be numerically predicted. The relative static state, which means that there is no relative motion between the superior and inferior bearing plates as shown in Fig. 3(a) during two or more consecutive time steps in numerical integration, is the main cause of residual displacement for SRB-LVDF. By setting $\ddot{x}_1$ in Eqs. (1) and (4) equal to zero, the critical characteristic strengths $F_{D,C}$ can be defined and calculated by Eqs. (6) and (7), respectively.

$$F_{D,C} = \left| \frac{1}{2}\left(M + m_1\right)\left[2\ddot{x}_g + g\left(\theta_1 + \theta_1\right)\mathrm{sgn}\left(x_1\right)\right] \right| \tag{6}$$

$$F_{D,C} = \left| \frac{1}{4}\left(M + m_1\right)\left(4\ddot{x}_g + \frac{g}{R}x_1\right) \right| \tag{7}$$

As can be seen form Eqs. (6) and (7), since the sloping angles in the slope rolling range and curvature radius in the arc rolling range have been determined, $F_{D,C}$ is only relevant to $\ddot{x}_g$. When the calculated value of $F_{D,C}$ is smaller than the designed friction damping force F_D at a specific time step (e.g., at t_i), the relative static state will occur. In other words, at the time step t_i, the values of $\ddot{x}_1$ and $\dot{x}_1$ are are equal to zero, and the value of x_1 is the same as that at the previous time step t_{i-1}.

The predicted horizontal acceleration and displacement response histories of SRB-LVDF1 and SRB-LVDF2 under El Centro, Kobe, TCU129, and AC156 are presented in Figs. 9-12, respectively, in which the quantitative information, including predicted maximum transmitted acceleration ($A_{\max,\,pred}$), predicted maximum isolation displacement ($D_{\max,\,pred}$), and predicted residual displacement ($D_{\mathrm{res},\,pred}$) are also provided. Two expedient representations to quantitatively evaluate the correlation between test results and numerical predictions, the coefficient of determination (R^2) and the author-defined energy dissipation ratio (*EDR*), which can be correspondingly calculated as per Eq. (8) and (9), are provided in Figs. 9-12 as well. Note that when the calculated values of R^2 and *EDR* are closer to one, a better correlation between test results and numerical predictions can be obtained.

$$R^2 = 1 - \frac{SSE}{SST} \tag{8}$$

$$EDR = \frac{W_{D,\,prediction}}{W_{D,\,test}} \tag{9}$$

where $SSE = \sum_{i=1}^{m}\left[\left(R_{test}\right)_i - \left(R_{prediction}\right)_i\right]^2$; $SST = \sum_{i=1}^{m}\left[\left(R_{test}\right)_i - \left(R_{test}\right)_{mean}\right]^2$; i is the data point at time t_i ; m is the total number of data points; R_{test} and $R_{prediction}$ are the experimental and predicted responses (acceleration or displacement), respectively. $\left(R_{test}\right)_{mean}$ is the mean of m sets of values of R_{test} ; and $W_{D,\,prediction}$ and $W_{D,\,test}$ are the predicted and experimental enclosed hysteresis loop areas, respectively.

As observed from the qualitative and quantitative comparison results, the proposed modified analytical model can provide a good match of the shaking table test results. Some critical responses, including maximum isolation displacement and maximum transmitted acceleration responses, basically, can be well captured. Even residual displacement responses in an order of 10^{-1} mm to 10^{0} mm can also be well approximated, in particular of the prediction results under El Centro and TCU129. Compared with displacement response histories and hysteresis loops, the numerical prediction accuracy in acceleration response histories might not be excellent, but still acceptable. It is because of frequent switches between the sticking and slipping phases of sliding friction motion during external disturbance (He *et al.* 2003), i.e., the breakaway friction effect becomes more significant (Constantinou *et al.* 1990).

4. Numerical comparison between SRB-CDF and SRB-LVDF

To have an insight into the merits and demerits of SRB-LVDF compared with SRB-CDF in the seismic control performance, if there are any, one SRB-CDF model (denoted as SRB-CDF-250 hereafter) and nine SRB-LVDF models (denoted as SRB-LVDF-50-50, SRB-LVDF-50-100, SRB-LVDF-50-150, SRB-LVDF-100-50, SRB-LVDF-100-100, SRB-LVDF-100-150, SRB-LVDF-150-50, SRB-LVDF-150-100, and SRB-LVDF-150-150, hereafter), whose quantitative design parameters and numerical hysteretic models are correspondingly detailed in Table 1 and illustrated in Fig. 13, are numerically examined. Except for the magnitude and variation slopes of friction damping force, the remaining design parameters, including the sloping angle of the rolling surfaces, the curvature radius of the arc rolling range, the seismic reactive mass and dimension of each component, etc., together with the total seismic reactive mass of the to-be-protected object above and the acceleration inputs, are identical to those adopted

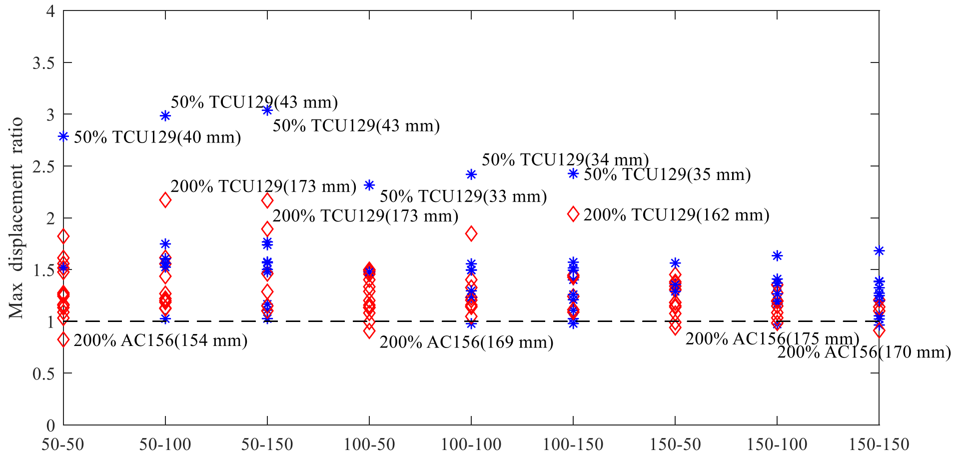

Fig. 15 Comparison of predicted maximum isolation displacement between SRB-CDF and SRB-LVDF modelst

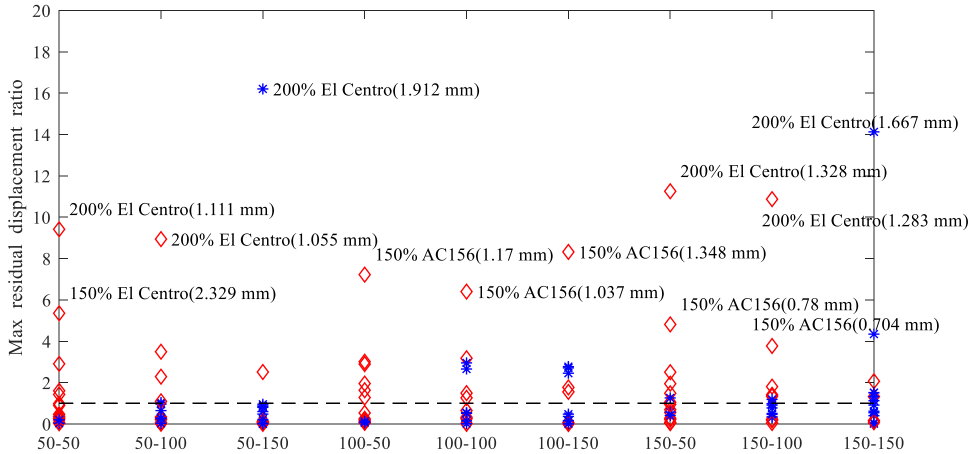

Fig. 16 Comparison of predicted residual displacement between SRB-CDF and SRB-LVDF models

for the experimental study on SRB-LVDF1 and SRB-LVDF2. It is assumed that the kinetic friction coefficient between the rubber and stainless materials adopted in these numerical hysteretic models is still approximated by a constant of 0.3. The number named in SRB-CDF-250 represents the designed constant friction damping force (with a unit of N). The first number named in the nine SRB-LVDF models represents the designed initial friction damping force (with a unit of N), and the second one represents the horizontal isolation displacement (or turning point, with a unit of mm) after exceeding which the linearly variable friction damping force will become larger than the constant one designed for SRB-CDF-250, i.e., 250 N. In other words, after the horizontal isolation displacement exceeds the turning point, i.e., x_1>50 mm for SRB-LVDF-50-50, SRB-LVDF-100-50, and SRB-LVDF-150-50, x_1>100 mm for SRB-CDF-50-100, SRB-LVDF-100-100, and SRB-LVDF-150-100), and x_1>150 mm for SRB-LVDF-50-150, SRB-LVDF-100-150, and SRB-LVDF-150-150), the horizontal acceleration transmitted to the protected object above the SRB-LVDF models will become larger than that above SRB-CDF-250. Generally, the smaller the initial friction damping force and the earlier the turning point designed, the larger the variation slope of the total friction damping force (when sgn(x_1)=1 and sgn($\dot{x}_1$)=1 or sgn(x_1)=-1 and sgn($\dot{x}_1$)=-1) obtained. When the designed variation slope of the total friction damping force (when sgn(x_1)=1 and sgn($\dot{x}_1$)=1, or sgn(x_I)=-1 and sgn($\dot{x}_1$)=-1) is not large sufficiently, the major portion of the total friction damping force will be contributed by the horizontal force component of the total normal force directed perpendicular to the sliding surface as shown in Figs. 4(b) and 5(b). Under this circumstance, the hysteretic behavior of SRB-LVDF will become slightly different from that shown in Fig. 5(d); for instance, SRB-LVDF-100-50, SRB-LVDF-100-100, SRB-LVDF-100-150, SRB-LVDF-150-50, SRB-LVDF-150-100, and SRB-LVDF-150-150, whose numerical hysteretic models as shown in Figs. 13(b) - 13(c) present the same direction of variation slopes of the total friction damping force when sgn(x_1)=1, sgn($\dot{x}_1$)=1 and sgn(x_1)=1, sgn($\dot{x}_1$)=-1 or when sgn(x_1)=-1, sgn($\dot{x}_1$)=-1 and sgn(x_1)=-1, sgn($\dot{x}_1$)=1. To have more numerical comparison results, more PA levels are considered for the unilateral acceleration inputs, as detailed in Table 2. The so-called near-fault pulse-like ground motions or those containing considerably abundant long period contents (Baker 2007, Jangid and Kelly 2001, Providakis 2008, Chopra and Chintanapakdee 2014, Shahbazi and Taghikhany 2017) are excluded in this preliminary numerical study.

The quantitative comparison, in terms of ratios of predicted maximum transmitted acceleration, maximum isolation displacement, and residual displacement responses of the SRB-LVDF models to those of the SRB-CDF model under each unilateral acceleration input as given in Table 2 are shown in Figs. 14 - 16, respectively. The data points presented in these figures are categorized into two groups: the predicted maximum isolation displacement is smaller and larger than the designed turning point, which are denoted by the blue * and red ◊ symbols, respectively. Or, the classification could be rationally imagined that the to-be-protected object is respectively subjected to frequent (or minor) and major earthquakes. As observed from Fig. 14, it is of no surprise that when the horizontal isolation displacement does not exceed the designed turning point, the SRB-LVDF models have a superior acceleration control performance to the SRB-CDF model, which is the major design purpose for SRB-LVDF in this study. It is particularly evident when designing a later turning point. This advantage is particularly important for some specific industries such as high-tech factories if remaining their functionality and quality control under frequent earthquakes rather than satisfying the same or other purposes under catastrophic earthquakes is their major concern for marketing competition. On the contrary, the larger the horizontal isolation displacement compared with the designed turning point, the worse the acceleration control performance; for instance, SRB-LVDF-50-50, SRB-LVDF-100-50, and SRB-LVDF-150-50 under 200% Kobe as shown in Fig. 14. In addition, when designing a larger value of initial friction damping force and a later turning point, i.e., a smaller variation slope of the total friction damping force (when sgn(x_1)=1 and sgn($\dot{x}_1$)=1 or sgn(x_1)=-1 and sgn($\dot{x}_1$)=-1), the acceleration control performance of the SRB-LVDF models is more convergent to the that of the SRB-CDF model.

As presented in Fig. 15, when the horizontal isolation displacement is either smaller or larger than the designed turning point, i.e., regardless of being subjected to minor or major earthquakes practically, in particular of the former, the displacement control performance of the SRB-LVDF models, in general, is inferior to that of the SRB-CDF model. It is evident when designing a smaller value of initial friction damping force and a later turning point, the former in particular. In other words, if the initial friction damping force is designed as a larger value, a larger hysteresis loop (or more precisely, a better energy dissipation capability) can be provided earlier so as to suppress the horizontal isolation displacement more effectively. However, meanwhile, it will also scarify the acceleration control performance especially when subjected to minor (or frequent) earthquakes. It should be noted that on the premise that the horizontal isolation displacement does not exceed the designed maximum displacement capacity, whether SRB-LVDF is more effective in suppressing displacement (or has a smaller displacement response) than SRB-CDF under the same external disturbance is not one of the design goals for SRB-LVDF in this study. Furthermore, when undergoing a larger displacement demand caused by earthquakes, e.g., SRB-LVDF-50-50, SRB-LVDF-100-50, SRB-LVDF-150-50, and SRB-LVDF-150-150 under 200% AC156 as shown in Fig. 15, it might have an opposite tendency to the observation aforementioned.

As shown in Fig. 16, the SRB-LVDF models under most of the unilateral acceleration input as given in Table 2 can exhibit a better re-centering performance (or have a smaller residual displacement response) than the SRB-CDF model, which is the other major design purpose for SRB-LVDF in this study. Although some exceptions present a ratio much larger than one, e.g., SRB-LVDF-50-150 and SRB-LVDF-150-150 under 200% El Centro as shown in Fig. 16, the absolute quantities of residual displacement can still be controlled as an order of 10^0 mm, which is still very satisfactory for the concerns of serviceability and functionality. In addition, the dependence of residual displacement on the designed initial friction damping force and turn point might be of less significance, which still needs more numerical or experimental results for further verification.

5. Conclusions

The practical feasibility of implementation of the linearly variable damping force design in a passive control manner into SRB, i.e., SRB-LVDF, is experimentally demonstrated in this study. A corresponding analytical model for SRB-LVDF is also proposed and its numerical predictions under different unilateral acceleration inputs are compared with the shaking table test results. Furthermore, the numerical results of SRB-LVDF are compared with those of SRB-CDF to further probe the advantages and disadvantages of SRB-LVDF. Some conclusions obtained based on the experimental and numerical comparison results of the designed models under the acceleration inputs considered are made as follows.

- By compressing the linear spring modules installed behind the rubber pads varied from the initial to maximum shortening, SRB can be designed with a function of linearly variable damping force in a passive control manner, i.e., SRB-LVDF. The experimental results of SRB-LVDF under different unilateral acceleration inputs, including three real earthquake records and one artificial acceleration history, present that the linearly variable damping force design performs as well as expected, i.e., the experimental damping force (or the transmitted horizontal acceleration) is linearly augmented with increasing the horizontal isolation displacement. Besides, very limited residual displacement after external disturbance presents that SRB-LVDF has a satisfactory re-centering performance.
- The qualitative and quantitative comparisons between the numerical predictions by the modified analytical model and the experimental results of SRB-LVDF present that the proposed analytical model is capable of capturing the actual horizontal dynamic behavior of SRB-LVDF very well, even for the prediction of residual displacement responses. In the future, if other more complicated functions for designing variable

damping force are adopted in SRB, a corresponding analytical model can also be obtained in the same manner as that used in this study. Accordingly, the efficacy of these new and different designs can then be more efficiently examined and demonstrated in a numerical manner, instead of an experimental manner.

• After experimentally and numerically verifying the practical feasibility of SRB-LVDF and the accuracy of the proposed analytical model, respectively, the seismic performance of several SRB-LVDF models with different damping force design parameters are numerically compared with that of an SRB-CDF model. The initial friction damping force designed for the SRB-LVDF models is smaller than the constant one for the SRB-CDF model. Based on the numerical comparison results under the acceleration inputs considered, it can be seen that when the horizontal isolation displacement does not exceed the designed turning point, i.e., the to-be-protected object is assumed to be subjected to frequent (or minor) earthquakes that seldom cause a very large displacement demand, the SRB-LVDF models, undoubtedly, have a superior acceleration control performance to the SRB-CDF model. It is particularly evident when designing a later turning point. In addition, with a larger value of initial friction damping force and a later turning point, the acceleration control performance of the SRB-LVDF models will be closer to that of the SRB-CDF model. More importantly, the SRB-LVDF models, in general, exhibit a better re-centering performance (or have a smaller residual displacement response) than the SRB-CDF model. The residual displacement responses of the SRB-LVDF models seem to be irrelevant to the designed initial friction damping force and turn point. However, the maximum horizontal displacement response of the SRB-LVDF models, especially when it is smaller than the designed turning point and a smaller value of initial friction damping force is designed, is larger than that of the SRB-CDF model.

• The preliminary experimental and numerical results provided in this study show that adopting SRB-LVDF might be suitable to meet some special performance requirements of high-tech factories, i.e., both remaining their functionality and process control under frequent (or minor) earthquakes and keeping their life safety under catastrophic earthquakes are equally important. However, the current experimental and numerical results might not be comprehensive sufficiently, and some questions extended from this research might deserve further study and clarification in the future. For instance, but not limited to the following, how to have a suitable SRB-LVDF design especially when subjected to the so-called near-fault pulse-like ground motions or those containing considerably abundant long period contents? Besides, as for the friction damping force design mechanism, if the breakaway friction effect is inevitable, even the effect is of insignificance, it is still required to be taken into consideration properly in the analytical model to have a more accurate and conservative prediction result for SRB-LVDF.

Acknowledgments

The study was financially aided by the Ministry of Science and Technology (MOST) of Taiwan [103-2221-E-492-005-], and was experimentally supported by the National Center for Research on Earthquake Engineering (NCREE), National Applied Research Laboratories (NARL) of Taiwan. The support is greatly acknowledged.

References

Abdollahzadeh G. and Darvishi R. (2017), "Cyclic behavior of DCFP isolators with elliptical surfaces and different frictions", *Struct. Eng. Mech.*, **64**(6), 731-736. https://doi.org/10.12989/sem. 2017.64.6.731.

AC156 (2010), Acceptance criteria for seismic certification by shake-table testing of nonstructural components. ICC Evaluation Service, LLC.

Baker, J.W. (2007), "Quantitative classification of near-fault ground motions using wavelet analysis", *Bull. Seismol. Soc. Amer.*, **97**(5), 1486-1501. https://doi.org/10.1785/0120060255.

Calvi, P.M., Moratti, M. and Calvi, G.M. (2008), "Seismic isolation devices based on sliding between surfaces with variable friction coefficient", *Earthq. Spectra*, **32**(4), 2291-2315. https://doi.org/10.1193/ 091515EQS139M.

Chai, J.F., Loh, C.H. and Sato, T. (2002), "Modeling of phase spectrum to simulate design ground motions", *J. Chinese Institute Eng.*, **25**(4), 447-459. https://doi.org/10.1080/02533839.2002. 9670719.

Chang, S.P., Makris, N., Whittaker, A.S. and Thompson, A.C.T. (2002), "Experimental and analytical studies on the performance of hybrid isolation systems", *Earthq. Eng. Struct. Dyn.*, **31**(2), 421-443. https://doi.org/10.1002/eqe.117.

Chopra, A.K. and Chintanapakdee, C. (2014), "Comparing response of SDF systems to near-fault and far-fault earthquake motions in the context of spectral regions", *Earthq. Eng. Struct. Dyn.*, **30**(12), 1769-1789. https://doi.org/10.1002/eqe.92.

Constantinou, M.C., Mokha, A. and Reinhorn, A. (1990), "Teflon bearings in base isolation II: modeling", *J. Structural Eng., ASCE*, **116**(2), 455-474. https://doi.org/10.1061/(ASCE)0733-9445 (1990)116:2(455).

Fenz, D.M. and Constantinou, M.C. (2006), "Behaviour of the double concave friction pendulum bearing", *Earthq. Eng. Struct. Dyn.*, **35**(11), 1403-1424. https://doi.org/10.1002/eqe.589.

Fenz, D.M. and Constantinou, M.C. (2008), "Modeling triple friction pendulum bearings for response-history analysis", *Earthq. Spectra*, **24**(4), 1011-1028. https://doi.org/10.1193/1.2982531.

Ghobarah, A. (2001), "Performance-based design in earthquake engineering: state of development", *Eng. Struct.*, **23**(8), 878-884. https://doi.org/10.1016/S0141-0296(01)00036-0.

Hadjian, A.H. (1982), "A re-evaluation of equivalent linear models for simple yielding systems", *Earthq. Eng. Struct. Dyn.*, **10**(6), 759-767. https://doi.org/10.1002/eqe.4290100602.

Harvey, Jr. P.S. and Kelly, K.C. (2016), "A review of rolling-type seismic isolation: historical development and future directions", *Eng. Struct.*, **125**(15), 521-531. https://doi.org/10.1016/j.engstruct.2016.07. 031.

He, W.L., Agrawal, A.K. and Yang, J.N. (2003), "Novel semiactive friction controller for linear structures against earthquakes", *J. Struct. Eng., ASCE*, **129**(7), 941-950. https://doi.org/10.1061/ (ASCE)0733-9445(2003)129:7(941).

Hwang, J.S. (1996), "Evaluation of equivalent linear analysis methods of bridge isolation", *J. Struct. Eng., ASCE*, **122**(8), 972-976. https://doi.org/10.1061/(ASCE)0733-9445(1996) 122:8(972).

Hwang, J.S., Huang, Y.N., Hung, Y.H. and Huang, J.C. (2004), "Applicability of seismic protective systems to structures with vibration sensitive equipment", *J. Struct. Eng.*, *ASCE*, **130**(11), 1676-1684. https://doi.org/10.1061/(ASCE)0733-9445(2004)130:11(1676).

Iwan, W.D. and Gates, N.C. (1979), "The effective period and damping of a class of hysteretic structures", *Earthq. Eng. Struct. Dyn.*, **7**(3), 199-221. https://doi.org/10.1002/eqe.4290070302.

Jangid, R.S. (2017), "Optimum friction pendulum system for near-fault motions", *Eng. Struct.*, **27**(3), 349-359. https://doi.org/10.1016/j.engstruct.2004.09.013.

Jangid, R.S. and Kelly, J.M. (2001), "Base isolation for near-fault motions", *Earthq. Eng. Struct. Dyn.*, **30**(5), 691-707. https://doi.org/10.1002/eqe.31.

Kasalanati, A., Reinhorn, A.M., Constantinou, M.C. and Sanders, D. (1997), "Experimental study of ball-in-cone isolation system", *The Proceedings of the ASCE Structures Congress XV*, Portland, Oregon, U.S.A, April.

Kelly, J.M. (1990), "Base isolation: linear theory and design", *Earthq. Spectra*, **6**(2), 223-244. https://doi.org/10.1193/1.1585566.

Lee, G.C., Ou, Y.C., Niu, T., Song, J. and Liang, Z. (2010), "Characterization of a roller seismic isolation bearing with supplemental energy dissipation for highway bridges", *J. Struct. Eng., ASCE,* **136**(5), 502-510. https://doi.org/10.1061/(ASCE)ST.1943-541X.0000136.

Makris, N. and Chang, S.P. (2000), "Effect of viscous, viscoplastic and friction damping on the response of seismic isolated structures", *Earthq. Eng. Struct. Dyn.*, **29**(1), 85-107. https://doi.org/10.1002/(SICI)10969845(200001)29:1<85::AIDEQE90 2>3.0.CO;2-N.

Panchal, V.R. and Jangid, R.S. (2008), "Variable friction pendulum system for near-fault ground motions", *Struct. Control Heal. Monit.*, **15**(4), 568-584. https://doi.org/10.1002/stc.216.

Ponzo, F.C., Cesare, A.D., Leccese, G. and Nigro, D. (2017), "Shake table testing on restoring capability of double concave friction pendulum seismic isolation systems", *Earthq. Eng. Struct. Dyn.*, **46**(14), 2337-2353. https://doi.org/10.1002/eqe.2907.

Providakis, C.P. (2008), "Effect of LRB isolators and supplemental viscous dampers on seismic isolated buildings under near-fault excitations", *Eng. Struct.*, **30**(5), 1187-1198. https://doi.org/10.1016/ j.engstruct.2007.07.020.

Shahbazi P. and Taghikhany T. (2017), "Sensitivity analysis of variable curvature friction pendulum isolator under near-fault ground motions", *Smart Struct. Syst.*, **20**(1), 23-33. https://doi.org/10.12989/sss. 2017.20.1.023.

Tadjbakhsh, I. and Lin, B.C. (1987), "Displacement-proportional friction (DPF) in base isolation", *Earthq. Eng. Struct. Dyn.*, **15**(7), 799-813. https://doi.org/10.1002/eqe.4290150702.

Tsai, M.H., Wu, S.Y., Chang, K.C. and Lee, G.C. (2007), "Shaking table tests of a scaled bridge model with rolling type seismic isolation bearings", *Eng. Struct.*, **29**(9), 694-702. https://doi.org/10.1016/ j.engstruct.2006.05.025.

Vargas, R. and Bruneau, M. (2009), "Experimental response of buildings designed with metallic structural fuses. II", *J. Struct. Eng., ASCE,* **135**(4), 394-403. https://doi.org/10.1061/(ASCE)0733-9445(2009)135:4(394).

Wang, S.J., Hwang, J.S., Chang, K.C., Shiau, C.Y., Lin, W.C., Tsai, M.S., Hong, J.X. and Yang, Y.H. (2014), "Sloped multi-roller isolation devices for seismic protection of equipment and facilities", *Earthq. Eng. Struct. Dyn.*, **43**(10), 1443-1461. https://doi.org/10.1002/eqe.2404.

Wang, S.J., Yu, C.H., Cho, C.Y. and Hwang, J.S. (2019), "Effects of design and seismic parameters on horizontal displacement responses of sloped rolling-type seismic isolators", *Struct. Control Heal. Monit.*, **26**(5). https://doi.org/10.1002/stc.2342.

Wang, S.J., Yu, C.H., Lin, W.C., Hwang, J.S. and Chang, K.C. (2017), "A generalized analytical model for sloped rolling-type seismic isolators", *Eng. Struct.*, **138**, 434-446. https://doi.org/10.1016/ j.engstruct.2016.12.027.

Wei B., Wang P., He X., Zhang Z. and Chen L. (2017), "Effects of friction variability on a rolling-damper-spring isolation system", *Earthq. Struct.*, **13**(6), 551-559. https://doi.org/10.12989/eas. 2017.13.6.551.

Yurdakul M. and Ates S. (2018), "Stochastic responses of isolated bridge with triple concave friction pendulum bearing under spatially varying ground motion", *Struct. Eng. Mech.*, **65**(6), 771-784. https://doi.org/10.12989/sem.2018.65.6.771.

KT